

BiCLIP: Bidirectional and Consistent Language–Image Processing for Robust Medical Image Segmentation

Saivan Talaei^{1*}, Fatemeh Daneshfar^{1*}, Abdulhady Abas Abdullah², and Mustaqeem Khan³^(✉)

¹ Department of Computer Engineering, University of Kurdistan, Iran
{s.talaei,f.daneshfar}@uok.ac.ir

² Artificial Intelligence and Innovation Centre, University of Kurdistan, Erbil, Iraq
abdulhady.abas@ukh.edu.krd

³ College of Information Technology, United Arab Emirates University, UAE
mustaqeemkhan@uaeu.ac.ae

Abstract. Medical image segmentation is essential for computer-assisted diagnosis and treatment planning, playing a key role in many real-world clinical workflows. Recently, multimodal vision-language methods have gained attention by leveraging textual descriptions to enhance semantic understanding. However, their robustness under realistic clinical conditions such as limited annotations and acquisition-related degradations remains insufficiently explored. We propose BiCLIP (Bidirectional and Consistent Language–Image Processing), a vision-language framework designed to improve robustness in medical image segmentation. BiCLIP introduces a bidirectional multimodal fusion mechanism that allows visual features to iteratively refine textual representations, strengthening semantic alignment. Additionally, an augmentation consistency objective regularizes intermediate representations across perturbed input views, promoting stable learning behavior. We evaluate BiCLIP on the QaTaCOV19 and MosMedData+ benchmarks, where it consistently outperforms strong image-only and multimodal baselines. Experiments show that BiCLIP remains robust when trained on only 1% of labeled data and withstands clinically motivated corruptions such as low-dose CT noise and motion blur.

Keywords: Text-Guided Medical Image Segmentation · Vision–Language Models · Robust Learning · Consistency Regularization

1 Introduction

Deep learning approaches have become central to medical image segmentation, facilitating automatic segmentation of anatomical structures and disease-related regions with an accuracy that is similar to expert annotations. Early convolutional architectures, including U-Net [1], were successful in integrating local

* These authors contributed equally to this work.

spatial details with global contextual information, leading to ubiquitous use in medical imaging applications. Despite this progress, purely image-only models still depend on image quality and acquisition conditions [5]. In addressing these limitations, text-guided segmentation approaches use linguistic information to form complementary semantic context and enhance the robustness and interpretability across diverse medical imaging tasks [4,6].

A growing body of work has investigated the integration of vision-language representations for medical image segmentation. Zhao et al. [7] propose Cap2Seg, which combines image captioning with lesion segmentation to produce textual descriptions for prediction without depending on external reports. As for foundation models, Hu et al. [9] present LGA, a lightweight language-guided adapter that provides textual embeddings to the Segment Anything Model with minimal fine-tuning. Wang et al. [10] develop an attribute-aware referring segmentation framework to improve robustness under missing textual prompts. In parallel to these efforts, Wang et al. [11] propose MedLangViT, which explores improved multimodal fusion, providing better integration between linguistic and visual cues for medical image segmentation.

Despite recent advances, existing vision-language segmentation methods often rely on a unidirectional fusion approach. In these methods, textual cues condition visual representations without allowing visual evidence to refine semantic cues. Additionally, they rarely incorporate explicit mechanisms to enhance robustness. As a result, learned representations may still be adversely affected by annotation scarcity and appearance variations. The method proposed here, BiCLIP, introduces a Bidirectional Multimodal Fusion (BMF) module that facilitates interaction between image and text representations in a bidirectional manner. Furthermore, an Image Augmentation Consistency (IAC) module regularizes intermediate features across perturbed inputs, thereby promoting robust representation learning.

Our contributions are summarized as follows. (1) We develop a BMF module that facilitates mutual exchange between visual and linguistic representations, enabling semantic cues to adapt in response to visual information. This interaction supports robustness in settings with limited supervision and degraded image quality, where static textual conditioning may be insufficient. (2) We introduce an IAC module that constrains intermediate features to remain consistent across both weak and strong perturbations, improving stability under appearance changes. (3) We conduct extensive robustness evaluations under low-annotation regimes and clinically motivated corruption settings, including simulated low-dose CT noise and motion blur, demonstrating the effectiveness of the proposed design choices.

2 Method

As shown in Fig. 1, BiCLIP processes a medical image and its associated text using parallel visual and textual encoders. The resulting embeddings are integrated through the proposed BMF module to form fused representations, which are used

to generate a pseudo image encoding cross-modal semantics. This pseudo image both refines the textual representation via a cycle-consistency objective and is concatenated with the original image for segmentation using a U-Net backbone. An IAC module further enforces representation stability under image perturbations. Details of each component are provided in the following subsections.

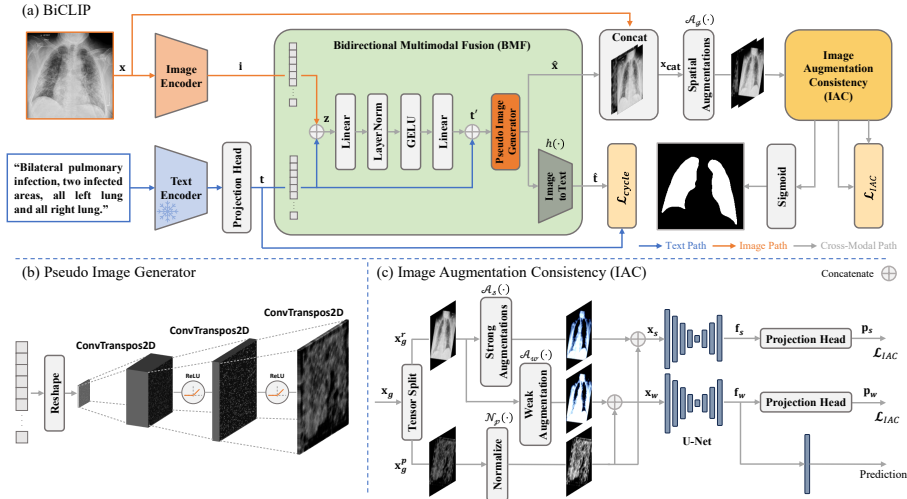


Fig. 1. Overview of the BiCLIP framework. (a) Overall multimodal segmentation architecture; (b) pseudo-image generator for bidirectional vision-language interaction; (c) IAC module for robust learning.

2.1 Bidirectional Multimodal Fusion Module

Given an input image of size $224 \times 224 \times 3$ and its associated clinical description, BiCLIP constructs aligned visual and textual representations for bidirectional multimodal fusion. The text is encoded using a frozen CXR-BERT model and projected to a compact text embedding, while the image is processed by a lightweight convolutional encoder to obtain a global visual embedding. These complementary embeddings serve as inputs to the proposed BMF module.

To enable image-aware language modeling, the BMF module allows visual information to refine the textual representation. The text embedding \mathbf{t} and image embedding \mathbf{i} are concatenated to form a joint multimodal representation $\mathbf{z} = [\mathbf{t}; \mathbf{i}]$, which aggregates semantic information from both modalities. This fused representation is passed through a multilayer perceptron $g_{BMF}(\cdot)$, which models cross-modal interactions and predicts a refinement term for the text embedding. The refined text embedding is then obtained via residual addition, preserving

the original linguistic structure while incorporating visual cues:

$$\Delta \mathbf{t} = g_{\text{BMF}}(\mathbf{z}), \quad \mathbf{t}' = \mathbf{t} + \Delta \mathbf{t}. \quad (1)$$

The refined text embedding \mathbf{t}' is then transformed into a pseudo image $\hat{\mathbf{x}}$ via a pseudo-image generator, which encodes cross-modal semantics and serves as an intermediate representation bridging language and vision; this generator is further supervised using a generated ground-truth signal to guide the pseudo-image formation. To close the bidirectional fusion loop, the pseudo image is mapped back into the text embedding space using an image-to-text head $h(\cdot)$, which projects visual content into the language embedding space, yielding the updated textual representation $\hat{\mathbf{t}}$. A cycle-consistency loss enforces alignment between the original and refined text embeddings,

$$\mathcal{L}_{\text{cycle}} = \|\mathbf{t} - \hat{\mathbf{t}}\|_2^2. \quad (2)$$

Finally, the pseudo image is concatenated with the original image and forwarded to a U-Net-based segmentation network for mask prediction.

2.2 Image Augmentation Consistency Module

Once the pseudo image $\hat{\mathbf{x}}$ is obtained, it is combined with the original image \mathbf{x} along the channel dimension to produce a multimodal input \mathbf{x}_{cat} . During training, two augmented variants of \mathbf{x}_{cat} are generated to improve robustness to appearance variations. To ensure spatial alignment between inputs and masks, a spatial augmentation function \mathcal{A}_g is applied jointly to the multimodal input and the segmentation mask \mathbf{y} :

$$(\mathbf{x}_g, \mathbf{y}_g) = \mathcal{A}_g(\mathbf{x}_{\text{cat}}, \mathbf{y}), \quad (3)$$

Two appearance-perturbed views are then generated from the augmented input \mathbf{x}_g . In particular, the real image component \mathbf{x}_g^r is processed with a weak augmentation \mathcal{A}_w and a strong augmentation \mathcal{A}_s to introduce different levels of appearance variation, while the pseudo image component \mathbf{x}_g^p is normalized using \mathcal{N}_p to serve as a stable semantic reference. After the weak and strong augmentations are applied, the resulting outputs are concatenated with the normalized \mathbf{x}_g^p :

$$\mathbf{x}_w = \text{concat}(\mathcal{A}_w(\mathbf{x}_g^r), \mathcal{N}_p(\mathbf{x}_g^p)), \quad \mathbf{x}_s = \text{concat}(\mathcal{A}_s(\mathbf{x}_g^r), \mathcal{N}_p(\mathbf{x}_g^p)). \quad (4)$$

These two augmented views are forwarded through the same U-Net backbone. Let $F(\cdot)$ denote the decoder feature map extracted from the final upsampling stage of the network. Accordingly, the weakly and strongly augmented inputs \mathbf{x}_w and \mathbf{x}_s yield the corresponding feature representations \mathbf{f}_w and \mathbf{f}_s , respectively,

$$\mathbf{f}_w = F(\mathbf{x}_w), \quad \mathbf{f}_s = F(\mathbf{x}_s). \quad (5)$$

These feature maps are projected into a compact embedding space using a lightweight projection head that applies global pooling followed by a linear transformation, producing \mathbf{p}_w and \mathbf{p}_s for the weakly and strongly augmented views. The IAC objective encourages agreement between these representations by minimizing their cosine distance,

$$\mathcal{L}_{\text{IAC}} = 1 - \frac{\mathbf{p}_w^\top \mathbf{p}_s}{\|\mathbf{p}_w\|_2 \|\mathbf{p}_s\|_2}, \quad (6)$$

thereby promoting stable and augmentation-invariant feature learning.

While the IAC module regularizes intermediate representations, the final segmentation prediction is produced from the weakly augmented branch by applying a 1×1 convolution followed by a sigmoid activation,

$$\hat{\mathbf{y}} = \sigma(\text{Conv}_{1 \times 1}(\mathbf{f}_w)), \quad (7)$$

which is used to compute the segmentation loss during training.

Overall Loss Function. The training objective of BiCLIP consists of a segmentation loss and several auxiliary losses that jointly regularize multimodal learning. The segmentation loss \mathcal{L}_{seg} is computed between the predicted segmentation map $\hat{\mathbf{y}}$ and the pixel-level ground-truth annotation \mathbf{y} using a Dice+Cross-Entropy formulation. An L_1 reconstruction loss \mathcal{L}_{gen} is applied between the generated pseudo image $\hat{\mathbf{x}}$ and its corresponding supervision signal to supervise the pseudo-image generator. In addition, the IAC and the cycle-consistency losses are incorporated to further regularize the training process. The overall training objective is therefore defined as

$$\mathcal{L}_{\text{total}} = \mathcal{L}_{\text{seg}} + \lambda_{\text{gen}} \mathcal{L}_{\text{gen}} + \lambda_{\text{IAC}} \mathcal{L}_{\text{IAC}} + \lambda_{\text{cycle}} \mathcal{L}_{\text{cycle}}, \quad (8)$$

where λ_{gen} , λ_{IAC} , and λ_{cycle} control the contribution of each auxiliary loss.

3 Experiments and Results

3.1 Settings

Datasets. We evaluate BiCLIP on two public medical image segmentation benchmarks, QaTa-COV19 and MosMedData+, which focus on COVID-19 chest CT segmentation. QaTa-COV19 contains 9,258 annotated CT images, split into 5,716 training, 1,429 validation, and 2,113 test samples. MosMedData+ includes 2,729 chest CT slices with pixel-wise annotations of lung abnormalities, divided into 2,183 training, 273 validation, and 273 test images.

Evaluation Metrics. We assess segmentation performance using the Dice coefficient and Intersection-over-Union (IoU), which are standard metrics for evaluating overlap between predicted masks and ground-truth annotations. Higher Dice and IoU values indicate better segmentation performance and closer agreement with the ground truth.

Implementation Details. All experiments were implemented in PyTorch and

conducted on a single NVIDIA RTX 4090 GPU. We trained the models using the AdamW optimizer with an initial learning rate of 1×10^{-4} and employed a cosine annealing warm restart scheduler to adapt the learning rate during training. The batch size was set to 16, and all models were trained for 150 epochs.

Table 1. Quantitative segmentation results on the QaTa-COV19 and MosMedData+ datasets. Best and second-best results are indicated by **bold** and underline.

Method	Venue	Text Backbone	QaTa-COV19		MosMedData+		
			Dice(%)	mIoU(%)	Dice(%)	mIoU(%)	
U-Net [1]	MICCAI'15	×	CNN	79.02	69.46	64.60	50.73
UNet++ [15]	MICCAI'18	×	CNN	79.62	70.25	71.75	58.39
nnU-Net [2]	Nature'21	×	CNN	80.42	70.81	72.59	60.36
UCTransNet [14]	AAAI'22	×	Hybrid	79.15	69.60	65.90	52.69
Swin-Unet [16]	ECCV'22	×	Hybrid	78.07	68.34	63.29	50.19
LAVT [17]	CVPR'22	✓	Hybrid	79.28	69.89	73.29	60.41
TGANet [18]	MICCAI'22	✓	CNN	79.87	70.75	71.81	59.28
LViT [3]	IEEE TMI'23	✓	Hybrid	83.66	75.11	74.57	61.33
Cap2Seg [7]	Frontiers'24	✓	Hybrid	81.32	71.61	75.87	63.02
RecLMIS [8]	IEEE TMI'24	✓	CNN	85.22	77.00	77.48	65.07
LGA [9]	MICCAI'24	✓	ViT	84.65	76.23	75.63	62.52
ARSeg [10]	MICCAI'25	✓	Hybrid	84.09	72.64	73.24	59.82
MedLangViT [11]	Electronics'25	✓	Hybrid	84.27	75.93	75.95	63.17
VT-MFLV [12]	Imaging'25	✓	CNN	83.34	72.09	75.61	63.98
EF-UNet [19]	arXiv'25	✓	CNN	<u>90.46</u>	<u>82.58</u>	<u>80.50</u>	<u>67.37</u>
SMF-net [13]	Frontiers'25	✓	Hybrid	85.78	76.45	78.70	64.17
BiCLIP (Ours)		✓	CNN	90.59	82.81	80.80	67.79

3.2 Comparison with State-Of-The-Art Methods

We compare BiCLIP with both unimodal and multimodal state-of-the-art segmentation methods on the QaTa-COV19 and MosMedData+ datasets. As shown in Table 1, BiCLIP achieves the best overall performance on both benchmarks. Compared with the strongest unimodal baseline, nnU-Net [2], BiCLIP improves Dice by over 10% on QaTa-COV19 and 8% on MosMedData+. Moreover, relative to recent multimodal methods such as RecLMIS [8], LGA [9], and MedLangViT [11], BiCLIP consistently achieves higher accuracy, with Dice gains of 3-6% and 2-4% on the two datasets, respectively. Fig. 2 further presents qualitative comparisons on clean and synthetically degraded test images. BiCLIP reduces segmentation errors such as missed or fragmented infection regions, with particularly improved delineation in ambiguous regions under noisy and blurred conditions. These improvements mainly stem from the BMF module, which integrates visual features with textual semantics to resolve ambiguous regions and refine segmentation quality.

3.3 Robustness Under Low-Data Regimes

To assess robustness under limited supervision, we progressively reduce the training data to 25%, 10%, 5%, and 1% while keeping all settings fixed, and compare BiCLIP with EF-UNet. As reported in Table 2, BiCLIP consistently outperforms EF-UNet in both Dice and mIoU across all data regimes, with particularly notable improvements in the more challenging 5% and 1% settings, highlighting its stable and reliable performance under extremely limited training data and severe annotation scarcity.

Table 2. Robustness comparison under different low-data training regimes.

Method	Regime	QaTa-COV19			MosMedData+		
		#Images	Dice(%)	mIoU(%)	#Images	Dice(%)	mIoU(%)
EF-UNet [19]	25%	1429	88.78	79.82	546	65.63	48.85
	10%	572	87.84	78.32	218	64.24	47.32
	5%	286	84.87	73.71	109	55.48	38.39
	1%	57	66.76	50.10	22	33.68	20.25
BiCLIP	25%	1429	88.78	79.83	546	72.18	56.48
	10%	572	87.14	77.21	218	68.29	51.85
	5%	286	84.92	73.79	109	64.71	47.83
	1%	57	74.79	59.73	22	46.49	30.29

3.4 Robustness to Noisy Test Data

To evaluate robustness under realistic test-time degradations, we apply two noise types to the test data. Low-dose CT noise is simulated via Poisson noise with dose levels 140, 120, and 110, where lower doses yield stronger noise. Motion blur is introduced using directional convolution kernels of sizes 3, 5, and 7, with larger kernels producing more severe blur to mimic patient motion during acquisition. **Low-dose CT noise.** As shown in Table 3, BiCLIP shows strong robustness across all dose levels. On QaTa-COV19, it achieves 81.90% Dice at Noise 140 and maintains clear gains at higher noise. Similar trends are observed on MosMedData+, where BiCLIP consistently achieves the highest Dice scores, indicating stable performance under increasing noise severity.

Motion blur. As reported in Table 3, BiCLIP remains robust to motion blur across all kernel sizes. It consistently achieves higher Dice scores than competing methods, even under severe blur. Comparable behavior is observed on MosMedData+, indicating that BiCLIP effectively handles spatial degradation and delivers reliable segmentation under motion-induced distortions.

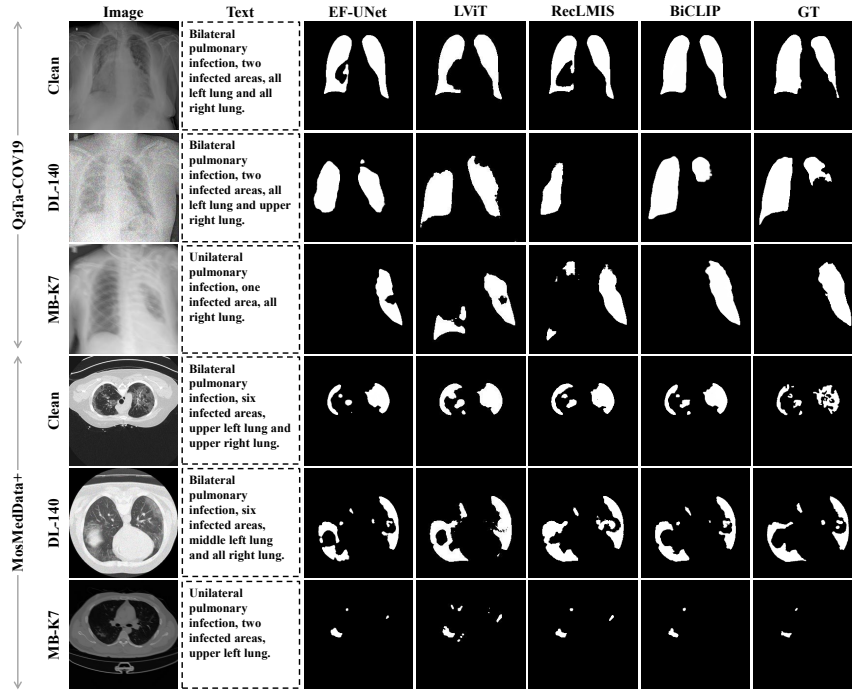


Fig. 2. Qualitative comparison of predictions on clean test images and on test images degraded by low-dose CT noise (DL-140) and motion blur (MB-K7; kernel size 7).

Table 3. Robustness comparison on noisy test data under low-dose CT noise and motion blur.

Method	Low-dose CT Noise					Motion Blur				
	Noise	QaTa-COV19		MosMedData+		Kernel	QaTa-COV19		MosMedData+	
		Dice	mIoU	Dice	mIoU		Dice	mIoU	Dice	mIoU
LViT [3]	140	70.07	58.65	54.57	43.75	K3	79.99	70.85	59.03	47.71
	120	68.27	56.71	54.19	43.28	K5	79.18	69.88	56.18	44.50
	110	67.60	55.95	52.68	41.95	K7	76.87	67.20	50.93	39.14
RecLMIS [8]	140	66.44	53.89	64.16	52.52	K3	82.65	73.80	76.77	64.15
	120	64.23	51.52	63.36	51.87	K5	82.70	73.79	75.60	62.61
	110	62.53	49.77	62.79	51.37	K7	81.56	72.29	71.86	58.21
EF-UNet [19]	140	<u>70.97</u>	<u>55.00</u>	<u>79.42</u>	<u>65.87</u>	K3	<u>89.51</u>	<u>81.01</u>	<u>80.49</u>	<u>67.35</u>
	120	<u>67.68</u>	<u>51.15</u>	<u>79.26</u>	<u>65.65</u>	K5	<u>88.76</u>	<u>79.80</u>	<u>80.15</u>	<u>66.88</u>
	110	<u>65.70</u>	<u>48.92</u>	<u>79.03</u>	<u>65.33</u>	K7	<u>87.20</u>	<u>77.31</u>	78.76	64.97
BiCLIP	140	81.90	69.35	80.40	67.22	K3	89.58	81.13	80.61	67.51
	120	78.03	63.97	80.33	67.12	K5	89.19	80.50	80.17	66.91
	110	74.84	59.79	80.26	67.02	K7	88.01	78.59	<u>77.97</u>	<u>63.89</u>

4 Conclusion

In this work, we introduce BiCLIP as a vision—language framework for robust medical image segmentation that combines bidirectional image–text interaction with consistency regularization. BiCLIP incorporates a BMF module for mutual refinement of visual and textual features and includes an IAC objective to stabilize intermediate representations under appearance perturbations. Extensive experiments demonstrate that BiCLIP is superior to strong unimodal and multimodal baselines. It achieves stable accuracy with limited supervision, and exhibits robustness to clinically relevant test-time corruptions, including low-dose CT noise and motion blur, underscoring its robustness and generalization capability in challenging medical imaging scenarios.

Acknowledgments. This research received no specific grant from any funding agency in the public, commercial, or not-for-profit sectors.

Disclosure of Interests. The authors have no competing interests to declare that are relevant to the content of this article.

References

1. Ronneberger, O., Fischer, P., Brox, T.: U-Net: Convolutional networks for biomedical image segmentation. In: Proc. MICCAI, LNCS, pp. 234–241 (2015)
2. Isensee, F., Jaeger, P.F., Kohl, S.A.A., Petersen, J., Maier-Hein, K.H.: nnU-Net: A Self-configuring Method for Deep Learning-based Biomedical Image Segmentation. *Nature Methods* (2021)
3. Li, Z., et al.: LVIT: Language meets vision transformer in medical image segmentation. *IEEE Trans. Med. Imaging* **43**(1), 96–107 (2023)
4. Zhou, H., Chen, S., Ma, J., et al.: MedCLIP-SAM: Bridging medical vision–language models and segment anything for universal medical image segmentation. In: Proc. CVPR, pp. 1–10 (2024)
5. Litjens, G., Kooi, T., Bejnordi, B.E., et al.: A survey on deep learning in medical image analysis. *Med. Image Anal.* **42**, 60–88 (2017)
6. Zhang, Y., Wang, X., Xu, M., et al.: Text-guided medical image segmentation via bidirectional multimodal adaptation. In: Proc. MICCAI, LNCS, pp. 1–11 (2024)
7. Zhao, W., Li, F., Diao, Y., et al.: Cap2Seg: Leveraging caption generation for enhanced segmentation of COVID-19 medical images. *Front. Phys.* **12**, 1439122 (2024)
8. Huang, X., Li, H., Cao, M., Chen, L., You, C., An, D.: Cross-modal conditioned reconstruction for language-guided medical image segmentation. *IEEE Trans. Med. Imaging* **43**, 1–12 (2024)
9. Hu, J., Li, Y., Sun, H., et al.: LGA: A language guide adapter for advancing the SAM model’s capabilities in medical image segmentation. In: Proc. MICCAI, LNCS **15012**, 610–620 (2024)
10. Wang, Q., Lin, X., Yan, Z.: Towards robust medical image referring segmentation with incomplete textual prompts. In: Proc. MICCAI, LNCS **15966**, 636–646 (2025)
11. Wang, Y., Su, J., Li, X., Nakahara, E.: MedLangViT: A language–vision network for medical image segmentation. *Electronics* **14**(15), 3020 (2025)

12. Wang, W., Li, J., Ye, Z., et al.: VT-MFLV: Vision–text multimodal feature learning network for medical image segmentation. *J. Imaging* **11**(12), 425 (2025)
13. Zhou, W., Shi, Z., Xie, B., et al.: SMF-Net: Semantic-guided multimodal fusion network for precise pancreatic tumor segmentation in medical CT. *Front. Oncol.* **15**, 1622426 (2025)
14. Wang, H., Cao, P., Wang, J., Zaiane, O.R.: UCTransNet: Rethinking the Skip Connections in U-Net from a Channel-wise Perspective with Transformer. In: *Proc. AAAI*, vol. 36, pp. 2441–2449 (2022)
15. Zhou, Z., Siddiquee, M.M.R., Tajbakhsh, N., Liang, J.: UNet++: A Nested U-Net Architecture for Medical Image Segmentation. In: *Proc. MICCAI Workshops (DLMIA), LNCS*, pp. 3–11 (2018)
16. Cao, H., Wang, Y., Chen, J., Jiang, D., Zhang, X., Tian, Q., Wang, M.: Swin-UNet: Unet-like Pure Transformer for Medical Image Segmentation. In: *Proc. ECCV, LNCS*, pp. 205–218 (2022)
17. Yang, Z., Wang, J., Tang, Y., Chen, K., Zhao, H., Torr, P.H.S.: LAVT: Language-aware Vision Transformer for Referring Image Segmentation. In: *Proc. CVPR*, pp. 18155–18165 (2022)
18. Tomar, N.K., Jha, D., Bagci, U., Ali, S.: TGANet: Text-guided Attention for Improved Polyp Segmentation. In: *Proc. MICCAI, LNCS*, pp. 151–160 (2022)
19. Chai, S., Jain, R.K., Xu, R., Mo, S., Hou, R., Teng, S., Liu, J., Lin, L., Chen, Y.-W.: A text-image fusion method with data augmentation capabilities for referring medical image segmentation. *arXiv preprint arXiv:2510.12482* (2025)